Effects of charge doping on Mott insulator with strong spin-orbit coupling, Ba2Na1−xCaxOsO6

Original
Effects of charge doping on Mott insulator with strong spin-orbit coupling, Ba2Na1−xCaxOsO6 / Cong, R.; Garcia, E.; Forino, P. C.; Tassetti, A.; Allodi, G.; Reyes, A. P.; Tran, P. M.; Woodward, P. M.; Franchini, C.; Sanna, S.; Mitrovic, V. F.. - In: PHYSICAL REVIEW MATERIALS. - ISSN 2475-9953. - 7:8(2023), pp. 084409.1-084409.16. [10.1103/PhysRevMaterials.7.084409]

Availability:
This version is available at: 11381/3004293 since: 2024-12-29T23:17:22Z

Publisher:
American Physical Society

Published
DOI:10.1103/PhysRevMaterials.7.084409

Effects of charge doping on Mott insulator with strong spin-orbit coupling, $Ba_2Na_{1-x}Ca_xOsO_6$

E. Garcia,[1] R. Cong,[1] P. C. Forino,[2] A. Tassetti,[2] G. Allodi,[3] A. P. Reyes,[4] P. M. Tran,[5] P. M. Woodward,[5] C. Franchini,[2] S. Sanna,[2] and V. F. Mitrović[1]
[1]*Department of Physics, Brown University, Providence, Rhode Island 02912, USA*
[2]*Department of Physics and Astronomy "A. Righi", University of Bologna, I-40127 Bologna, Italy*
[3]*Dipartimento di Scienze Matematiche, Fisiche e Informatiche, Universitá di Parma I-43124 Parma, Italy*
[4]*National High Magnetic Field Laboratory, Tallahassee, Florida 32310, USA*
[5]*Department of Chemistry and Biochemistry, The Ohio State University, Columbus, Ohio 43210, USA*
(Dated: June 29, 2023)

The effects of doping on the electronic evolution of the Mott insulating state have been extensively studied in efforts to understand mechanisms of emergent quantum phases of materials. The study of these effects becomes ever more intriguing in the presence of entanglement between spin and orbital degrees of freedom. Here, we present a comprehensive investigation of charge doping in the double perovskite Ba_2NaOsO_6, a complex Mott insulator where such entanglement plays an important role. We establish that the insulating magnetic ground state evolves from canted antiferromagnet (cAF) [1] to Néel order for dopant levels exceeding $\approx 10\%$. Furthermore, we determine that a broken local point symmetry (BLPS) phase, precursor to the magnetically ordered state [1], occupies an extended portion of the $(H-T)$ phase diagram with increased doping. This finding reveals that the breaking of the local cubic symmetry is driven by a multipolar order, most-likely of the antiferro-quadrupolar type [2, 3].

Introduction

Intricate interplay between strong electron correlations, and intertwined spin and orbital degrees of freedom leads to many diverse complex quantum phases of matter [4–7]. Often, correlations of the spin and orbital degrees of freedom can be treated on distinct energy scales. However, this is not the case in systems containing $5d$ transition-metal ions, where spin-orbit coupling (SOC) and electron correlations are comparable in size [5, 8–14]. As a result, $5d$ compounds exhibit a wide range of exotic magnetic properties, structural distortions, and multipolar ordering [1, 3, 4, 15–21]. The underlying physical ground state, is controlled by the multiplet structure of the constituent ions, the nature of the chemical bonds in the crystal, and its symmetry. This complexity often leads to intricate quantum "hidden" orders, elusive to most standard experimental probes. Nevertheless, the structural, magnetic, and electronic properties can be finely tuned by altering the degeneracy of a multitude of ground states varying external perturbations, such as pressure, strain and doping [20, 22–24].

The expectation, under the simplest picture, is that Mott insulators with integer number of electrons per site favor an antiferromagnetic ground state (AFM), and that charge doping leads to a metal-insulator transition (MIT) into a conducting state [25]. The most notable example of doping is the superconducting state in cuprates believed to emerge from a parent antiferromagnetic Mott state [26–28]. Specifically, as doping increases, antiferromagnetism gives way to exotic orders such as "stripe", unidirectional charge density wave, spin density wave, and unconventional d-wave superconductivity and with high enough doping the system becomes a Fermi liquid [26, 28, 29]. In addition to this well known class of MITs induced in Mott insulators by Coulomb interactions [26, 27, 30–32], insulators purely driven by spin correlations have been recently observed [33]. Yet another interesting case arises in Mott insulators when a strong SOC locally entangles the spin and orbital degrees of freedom. In such systems unconventional quantum magnetic and multipolar orders may stabilize [5, 6, 17, 18, 22]. Furthermore, the effects of charge doping are expected to be strikingly different than in systems where SOC can be treated as a perturbation to electronic correlations [5, 34–40], because multipolar orbital order and/or complex multi-orbital arrangements favor charge localization. A representative material of such Mott insulators is the $5d^1$ double perovskite Ba_2NaOsO_6 [41, 42] that evolves to the $5d^2$ configuration upon charge doping.

This $5d^1$ Os^{7+} Mott insulator displays a seemingly contradictory combination of a weak ferromagnetic moment ($\sim 0.2\ \mu_B$ / formula unit) below $T_C \approx 6.8$ K and a negative Weiss temperature [43]. Its weak moment at low temperature derives from an exotic canted-antiferromagnetic (cAFM) phase that is preceded by a broken local point symmetry (BLPS) state [1, 44, 45]. Fully doped, Ba_2CaOsO_6, on the other hand, is a $5d^2$ Os^{6+} Mott insulator that possibly hosts a complex ferro-octupolar order instead of a simple Néel AF order [17, 21, 46, 47]. Interestingly, recent theoretical work reveals different types of multipolar orders in $5d^2$ Mott insulators, such as ferri-octupolar [48], ferro-octupolar [22, 49], and antiferro-quadrupolar ordering [2, 3]. Microscopic study of the magnetic and structural properties

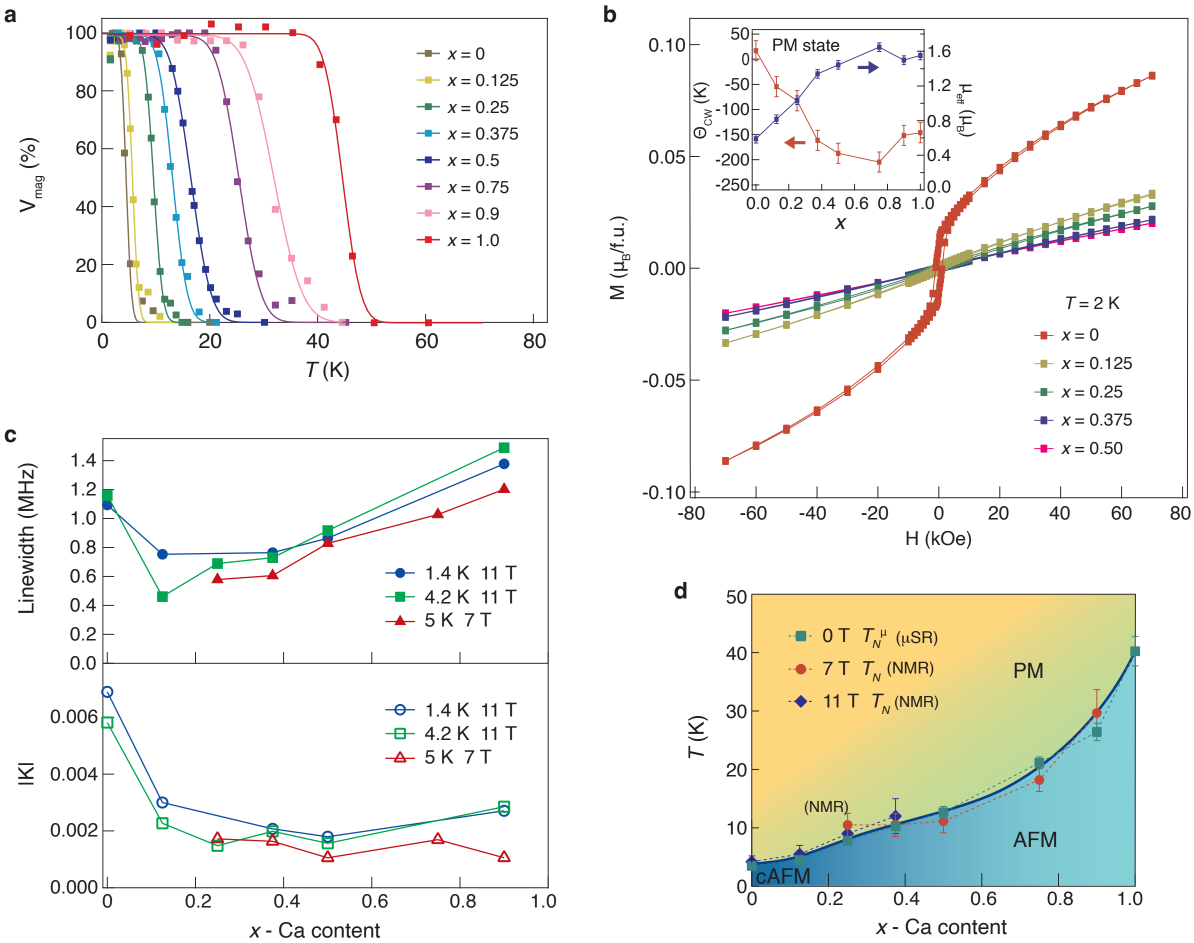

FIG. 1. **Magnetic state evolution as a function of charge doping (x) in $Ba_2Na_{1-x}Ca_xOsO_6$.** **(a)** Magnetic volume fraction extracted from μSR asymmetry for all doping levels. The magnetic transition temperature is defined as the 90% filling of the magnetic volume and increases monotonically with increasing Ca doping. **(b)** Magnetization as a function of applied magnetic field at 2 K. The results of high temperature ($T \gtrsim 50$ K) Curie Weiss fittings for magnetic susceptibility measurements in the PM state are shown in the inset. **(c)** ^{23}Na NMR spectral linewidth (top) and absolute value of Knight shift (bottom) as a function of doping concentration at various temperatures. **(d)** Magnetic phase diagram. Markers denote magnetic transition to the canted AFM and collinear AFM state for zero-field μSR and high field NMR measurements. Solid line serves as a guide to the eye. Typical error bars are on the order of a few percent and not shown for clarity in panels **a - c**.

of the double-perovskite $5d$ compounds with cubic symmetry, as presented here, provides essential guidance for the development of the relevant theoretical framework for the description of Mott insulators with strong SOC. Once identified, such a theoretical framework can be extended to more intricate lattices, such as the honeycomb and/or triangular lattice, where novel types of exotic quantum orders can be stabilized [2, 5, 14].

Here, we present a comprehensive study of the effect of charge doping on a Mott insulator with both strong electron correlations and SOC, represented by the double perovskite Ba_2NaOsO_6, from $5d^1 \rightarrow 5d^2$. Specifically, we investigate the magnetic field-temperature (H–T) phase diagram evolution as a function of charge doping (x) achieved by Na^+/Ca^{++} heterovalent substitution in $Ba_2Na_{1-x}Ca_xOsO_6$, employing magnetic resonance techniques. We find that the system remains insulating at all doping levels, implying that the dopants form an inhomogeneous electronic state. We compiled a magnetic and structural phase diagram for dopant concentrations ranging from $x = 0 \rightarrow 1$. The insulating magnetic ground state evolves from canted antiferromagnetic (AF) [1] to Néel nearly-collinear AF state (hereafter referred to as collinear AF state for brevity) for dopant levels exceeding $\approx$ 10%. Analyzing the complex broadening of the ^{23}Na NMR spectra, which onsets well above the magnetic transition, and temperature dependence of NMR shift, we establish that a cubic to orthorhombic local distortion of the O-octahedra is present for all compositions [50, 51]. The local distortion is the signature of a BLPS phase, identified as a precursor to the magnetic state in the single crystals of Ba_2NaOsO_6 [1], and not a trivial

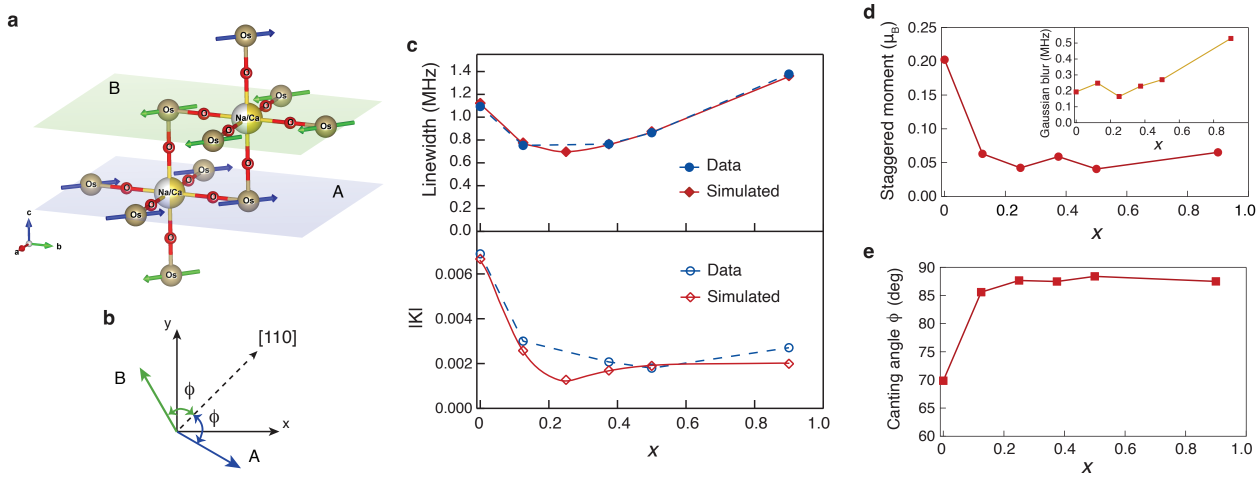

FIG. 2. **Doping evolution of the staggered moment in the low temperature magnetic state.** **(a)** Schematic of the spin model used to fit the NMR observables. Different colors of the arrows denote different spin environments at the Os sites. The two planes with distinctly oriented moments from sub-lattice A and B are shown in different shades. **(b)** Schematic of the canted spin arrangement by angle ϕ with respect to the [110] direction in the XY plane. **(c)** Simulated and measured NMR spectra linewidth and Knight shift at $T = 1.4$ K and $H = 11$ T as a function of Ca doping x in $\mathrm{Ba_2Na_{1-x}Ca_xOsO_6}$. **(d)** Simulated evolution of the staggered moment, defined as the projection of moments from two sub-lattices, A and B, along the applied field, as a function of doping in the magnetic state. The Gaussian blur, used to properly account for magnetic broadening, of simulated spectra is shown in the inset. The blur increases abruptly for $x = 0.9$. This might be related to the increased inhomogeneity of the local magnetic field environment at the Na nuclei site. Details of this simulation can be found in Supplementary Note 6. **(e)** Simulated evolution of the canted angle, defined as the angle between the sub-lattice FM spin orientation and the [110] easy axis, as a function of doping in the magnetically ordered state. Typical error bars are on the order of a few per cent and not shown for clarity. Solid and dashed line serves as guide to the eye.

consequence of a simple structural phase transition. The observation of the breaking of the local cubic symmetry and concurrent development of the NMR shift anisotropy for the entire range of dopings investigated implies that this symmetry breaking is driven by a multipolar order, most-likely of the antiferro-quadrupolar type [2, 3]. Remarkably, we find that the cubic to orthorhombic local distortion occurs independently of the exact nature of the low temperature magnetic state, signaling that the presence of canted moments is not the sole consequence of the BLPS [52]. In summary, our findings evidence that local distortions persist in the doped samples and that they favor the onset of an antiferro-quadrupolar order.

Results

We now describe details of our systematic study of $\mathrm{Ba_2Na_{1-x}Ca_xOsO_6}$ through the partial heterovalent substitution of monovalent Na with divalent Ca for $0 \leq x < 1$, performed to better understand the effects of doping and to elucidate the competing interactions that drive distinct magnetic ground states utilizing muon-spin relaxation (μSR), nuclear magnetic resonance (NMR), and magnetization measurements. We found that the insulting state persists at all doping concentrations despite the injection of electrons and an evolution into the AFM state. This finding is based on thorough examination of the response of the NMR resonant circuit.

Magnetic state - μSR magnetic volume fraction. First, we consider the evolution of the magnetic ground state of $\mathrm{Ba_2Na_{1-x}Ca_xOsO_6}$ as a function of the Na/Ca substitution ($0 \leqslant x \leqslant 1$) as probed by zero field muon spin relaxation (ZF-μSR) measurements. In the absence of an external field ($H = 0$ T), the spin $I = 1/2$ muon implanted in the sample precesses around the spontaneous local magnetic field arising from the magnetically ordered state at the muon site. The muon precessions are reflected in damped oscillations of the muon asymmetry decay, probing the fraction of precessing muons, which in turn is proportional to the magnetic volume (see methods). Our ZF-muSR asymmetry measurements for the end members $x = 0$ and 1 are in agreement with those previously reported in Refs. [42, 48]. In Fig. 1a, we plot the temperature evolution of the magnetic volume fraction V_{mag} as a function of doping. We find that samples of all concentrations display a magnetic transition as the volume fraction approaches 100% in the low temperature limit. The transition temperature into a magnetically ordered state, T_N^{μ}, defined to be at $V_{mag} = 90\%$, grows monotonically from approximately $T = 5$ K to 40 K as increasing doping induces a configuration change from the $5d^1$ to the $5d^2$ [23], as illustrated in Fig. 1d.

Magnetic state - magnetization. We have also performed magnetization measurements to get a better insight into the nature of the magnetic transitions observed through ZF-μSR. In Fig. 1b, we plot magnetiza-

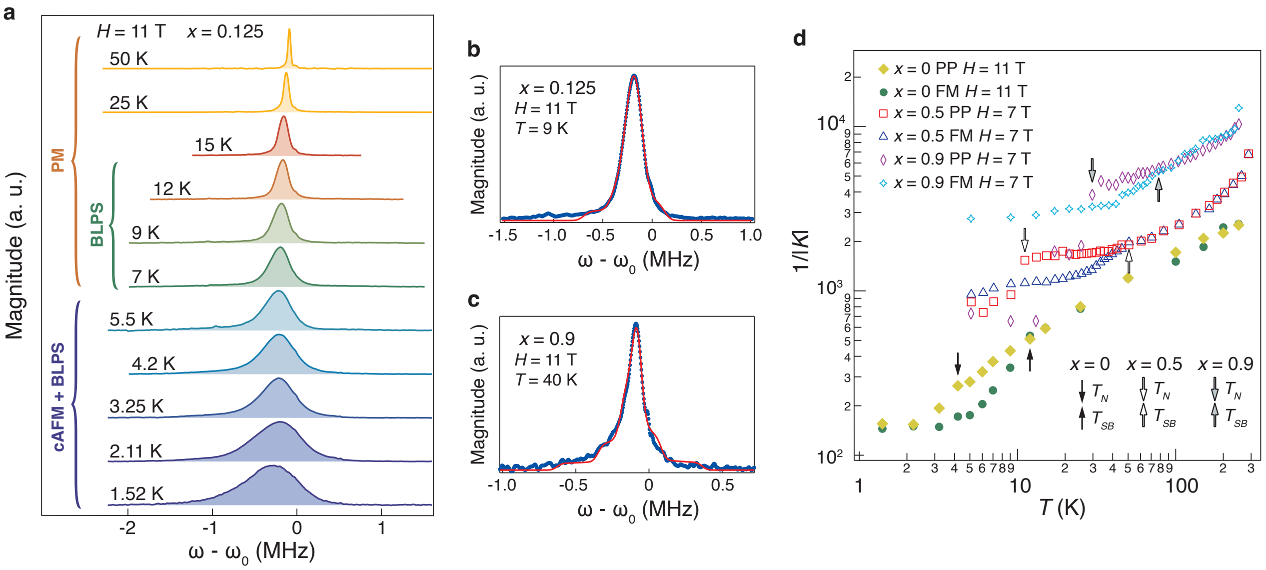

FIG. 3. **NMR spectral evidence of broken local point symmetry.** **(a)** Temperature evolution of ^{23}Na spectra for x=0.125 at H = 11 T. ^{23}Na powder NMR spectrum simulation results at H = 11 T for **(b)** x = 0.125 and **(c)** x = 0.9 in the BLPS phase. **(d)** Representative NMR Knight shift as a function of temperature at 11 T and 7 T. Arrows indicate the corresponding structural T_{SB} and magnetic T_N transition temperatures. $x = 0.9$ (Ca=90%) data is vertically offset for presentation clarity. Typical error bars are on the order of a few per cent and not shown for clarity.

tion curves as a function of an applied magnetic field for $T = 2$ K. The $x = 0$ sample displays a non-linear field dependence with a characteristic S shape and a small hysteretic behavior consistent with a moderately weak ferromagnetic character due to the significant moment canting in the cAFM phase. This is in agreement with the magnetization behavior observed in $\mathrm{Ba_2NaOsO_6}$ single crystals [43]. This hysteretic behavior is rapidly suppressed with charge doping and is effectively undetectable for doping exceeding $x \sim 0.1$. Magnetic susceptibility measurements were performed as a function of temperature at $H = 0.1$ T for all samples. The resulting magnetic susceptibility in the high temperature paramagnetic (PM) region fits well to a Curie-Weiss (CW) function plus a small temperature independent contribution. The resulting CW temperature (θ_{CW}) and effective moment per formula (μ_{eff}) are displayed in the inset to Fig. 1b. The values of the end members are in very good agreement with those previously reported for $\mathrm{Ba_2Na_{1-x}Ca_xOsO_6}$ at $x = 0$ ($\mu_{\mathrm{eff}} = 0.6\mu_B$) and $x = 1$ ($\mu_{\mathrm{eff}} = 1.6\mu_B$)[41, 43, 46, 47]. Furthermore, the extracted effective moments increase smoothly as the system evolves from the $5d^1$ to $5d^2$ configuration, while θ_{CW} becomes more negative. The extracted effective moment for both configurations is significantly suppressed from the theoretical value expected if SOC were negligible ($\mu_{\mathrm{eff}} = 1.73\,\mu_B$ and $\mu_{\mathrm{eff}} = 2.83\,\mu_B$ for $5d^1$ to $5d^2$ configurations, respectively) and is closer to the expected moments in the infinite SOC limit ($\mu_{\mathrm{eff}} = 0\mu_B$ and $\mu_{\mathrm{eff}} = 1.25\mu_B$ for $5d^1$ and $5d^2$ configurations, respectively) [8, 9, 53]. The experimentally determined values of μ_{eff} being significantly reduced from those expected for negligible SOC limit indicates the presence of strong SOC (in agreement with predicted SOC coupling lambda ~ 0.3 eV), while their being larger than those in the limit of infinite SOC can be attributed to the hybridization of Os d and oxygen p orbitals, with extra moments coming from the p orbitals, in agreement with predictions of Ref. [54]. The most likely origin of the observed effective moment increase with doping ($5d^1 \to 5d^2$) is the enhancement of the spin quantum number. This is because the spin (S) is predicted to increase from $S = 1/2$ to $S = 1$ as doping changes from $x = 0 \to x = 1$ [54].

Magnetic state - NMR. In order to obtain insight into the microscopic nature of the magnetically ordered state throughout the doping evolution, we performed detailed analysis of the ^{23}Na NMR spectra (see Methods). That is, we analyzed how the spectral shape changes in the magnetically ordered state, *i.e.* measured below T_N, as a function of the Ca content x. In Fig. 1c, we plot the absolute value of the Knight shift, deduced from first moment of the NMR spectra, and the linewidth of the spectra as a function of x. The magnitude of the Knight shift rapidly decreased on introduction of Ca dopants ($x > 0$) and remains nearly constant for higher doping ($x \geqslant 0.1$). The absolute value of the shift is a measure of the local magnetic moment projected along the external magnetic field direction. In the magnetically ordered canted state, the shift is proportional to the projection of the non-compensated magnetic moment along the applied magnetic field, as was demonstrated by ^{23}Na NMR measurements on $\mathrm{Ba_2NaOsO_6}$ single crystals [1, 44]. Therefore, the observed abrupt decrease of the shift upon the introduction of dopants indicates that the addition of charge effectively quenches the FM component, while further doping ($x \geqslant 0.1$) leads to a more uniform distribution of the projected moments. Furthermore upon the introduction of dopants ($x > 0$), the linewidth, which reflects the distribution of the magnetic fields projected along the applied magnetic field, exhibits the same abrupt decrease as the NMR shift, in agreement with the suppression of the canted nature of the magnetic order upon charge doping. In the collinear AFM state, the spectral linewidth is qualitatively proportional to the size of the local ordered magnetic moment. Thus, the smooth increase of the linewidth observed for $x > 0.1$ in Fig. 1c, indicates a progressive rise of the ordered magnetic moment as the charge concentration approaches $x = 1$, *i.e.* the $5d^2$ configuration (full quantitative analysis of the linewidth is presented in the next section). We point out that one would naively expect that the linewidth monotonically increase with doping since it introduces inhomogeneity in the crystal, which is not what was observed here because the NMR linewidth reflects intrinsic inhomogeneities of the magnetic ground state. Both the magnetization and the low temperature NMR measurements are consistent with a picture where the canted magnetic state rapidly evolves into the collinear AFM phase upon the introduction of charge and that the ordered magnetic moment increases as a function of Ca doping.

Microscopic nature of the magnetic state. To investigate the direct effect of doping on the nature of the staggered magnetic moments, *i.e.* a two sublattice canted antiferromagnetic order observed in $\mathrm{Ba_2NaOsO_6}$ single crystal [1], we have simulated the powder spectrum corresponding to the two sublattice cAF order identified in Ref. [1] (Methods). The input parameters for the simulations include the electronic spin moment ($\vec{S}$) and the hyperfine coupling tensor ($\mathbb{A}$). For each Ca doping concentration, we fix the value of $\vec{S}$ to be that of the effective moment ($\vec{S} = \mu_{\text{eff}}$) deduced from susceptibility measurements (the inset to Fig. 1b). Simulated spectra are then fitted to the observed ones with canting angle, and consequently staggered moment, as a fitting parameter. Here, the canting angle is that between the sub-lattice FM spin orientation and the [110] easy axis, while the staggered moment refers to the projection of the moments from the two sub-lattices, A and B, along the applied field direction. The simulation results are summarized in Fig. 2. We find that both, the canting angle and the staggered moment, change abruptly upon charge doping for $x > 0.1$. For $x = 0$, we obtain the best fit for a canting angle of 68°, consistent with that reported for pure $\mathrm{Ba_2NaOsO_6}$ single crystal [1]. For $x > 0.1$, the canting angle rapidly approaches 90°, the value associated with a collinear AFM state (see Fig. 2d). The deduced canting angles and staggered moments serve as input parameters to calculate the doping evolution of the Knight shift and linewidth associated with the local spin arrangement depicted in Fig. 2a. The calculated evolution of the shift and the linewidth is in an excellent agreement with observations, as shown in Fig. 2c. As x increases, the Knight shift decreases as a direct consequence of the increase of the canting angle, as depicted in Fig. 2b. On the other hand, the linewidth decrease with increasing x is associated with the weakening of the off-diagonal components of the hyperfine coupling tensor, for the canting angle $\sim 90°$. Furthermore in the inset to Fig. 2d we plot the Gaussian blur, which is used to account for the inhomogeneous magnetic broadening of the measured spectra, and its abrupt increase with doping approaching $x \to 1$ indicates that injected charge is inhomogeneously distributed.

Broken local point symmetry (BLPS). Next, we investigate the effect of charge doping on the BLPS phase [1]. The onset temperature of the visible broken local point symmetry is determined from the NMR Knight shift. We then proceed to analyze NMR powder spectral shapes at temperatures above the transition to the magnetically ordered state to determine the nature of the local crystal symmetry.

This subtle symmetry breaking has eluded previous diffraction measurements [43], but is well reflected in the distortion of the NMR spectra by the unbalanced spectral weight distributed towards a lower frequency with respect to its main peak associated with the cubic symmetry. A direct phenomenological way to detect and estimate the distortion of the spectra is by comparing the temperature evolution of the frequency of the peak position of the spectra to the first moment of the frequency distributions. In Fig. 3d, we display representative data sets for the comparison of the Knight shift obtained relative to the frequency ω^i of the first moment ($i = fm$) and peak ($i = pp$) of our NMR spectral lines (see Methods). The clear bifurcation in $1/|K|$ between the shift obtained by using the peak position and first moment marks the structural phase transition to the BLPS phase, T_{SB}. Upon further cooling, a sharp drop of $1/|K|$ is observed, denoting the transition temperature T_N into the magnetic state (see Methods). The magnetic transition temperature, T_N, obtained from the $1/|K^{pp}|$ drop, is consistent with that determined from the peak of the NMR relaxation rate (not shown) and from ZF-muSR measurements (Fig. 1d). These observations indicate that below T_N, an AF order is formed. In an AF ordered state, net projected moment along the applied field is significantly reduced, and vanishes in the case of collinear AF order, resulting in the observed drop in the Knight shift.

Nature of the broken symmetry. In Fig. 3a, we plot ^{23}Na NMR spectra of $\mathrm{Ba_2Na_{1-x}Ca_xOsO_6}$ for $x = 0.125$ at 11 T. The cubic paramagnetic (PM) state is characterized by the narrow symmetric spectra, as expected in the highly symmetric cubic PM phase. The BLPS arises in the intermediate temperature range and is marked by asymmetric spectra with a more pronounced tail at lower

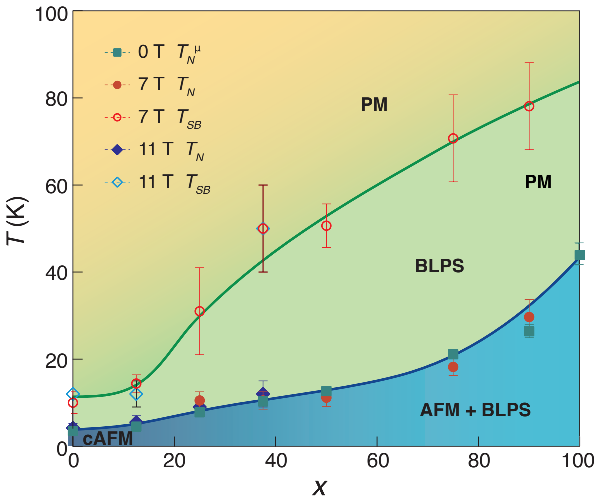

FIG. 4. **Phase diagram of $\mathbf{Ba_2Na_{1-x}Ca_xOsO_6}$.** Solid markers denote the magnetic transition to the canted AFM and collinear AFM state for zero-field μSR and high field NMR measurements. Open markers denote structural transitions into the BLPS phase. Solid lines serve as a guide to the eye.

frequencies. At low temperatures, in the magnetically ordered phase, the BLPS phase coexists with magnetism revealed by asymmetry of the NMR spectra. As elaborated in the Supplementary Note 4, a cubic local environment at the nuclear site must lead to a symmetric spectrum, while only non-cubic local symmetries, such as tetragonal or orthorhombic, can generate asymmetric lineshapes. We have performed detailed simulations of the ^{23}Na NMR powder pattern spectra in the presence of a quadrupolar interaction with the electric field gradient (EFG) and an anisotropic Knight shift $\mathbb{K}$ (see Methods & Supplementary Note 4), following the notation of [55]. We find that above T_N, in the PM & BLPS phases, the resulting powder NMR spectra must reflect the symmetry of the $\mathbb{K}$ and EFG tensors. Therefore, the shape of the NMR spectra provides precise information about any deviation from the cubic symmetry. Indeed, our systematic analysis of the measured spectra demonstrates that the best fits can only be achieved by using orthorhombic distortions, in agreement with findings in Ba_2NaOsO_6 single crystals [1].

In Fig. 3b & 3c we illustrate representative results of our ^{23}Na NMR powder spectra simulations in the BLPS phase (details of the simulation are given in Supplementary Note 4). By fitting the powder spectra, we deduce that the EFG and $\mathbb{K}$ tensors are orthorhombic and collinear to one another. These findings reveal that the main signature of the BLPS phase is not only the cubic symmetry breaking, but also the concurrent development of a collinear $\mathbb{K}$ anisotropy, indicating that the BLPS is a consequence of a multipolar order formation. That is, the deduced $\mathbb{K}$ anisotropy implies that the BLPS does not consist of a simple structural distortion but rather involves distortions of magnetic super-exchange paths, plausibly induced by a formation of a multipolar ordering. Therefore, the BLPS is most likely an anisotropic multipolar phase.

Phase diagram. Both T_{SB} and T_N obtained from ^{23}Na NMR at 7 T and 11 T are displayed in the temperature versus doping phase diagram plotted in Fig. 4. The results show that the BLPS phase, a precursor to the magnetic state, is an intrinsic characteristic of these Mott-insulating metal oxides and persists to higher temperature, up to about 80 K, when approaching the $5d^2$ configuration. This orthorhombic local point distortion of the octahedra is a clear signature that these materials are intrinsically dominated by low temperature anisotropic spin-lattice interactions, an essential ingredient to be included in any microscopic quantum theory of Dirac-Mott insulators.

Discussions

We have performed a microscopic investigation of the transformation of a $5d^1$ double perovskite Mott insulator into a $5d^2$ configuration by charge doping. We observed that the system remains insulating while the NMR linewidth (Gaussian blur) increase as doping approaches $x \to 1$. These findings indicate that the injected charges are not uniformly distributed into the $5d^1$ double perovskite, rather they are inhomogeneously trapped, most likely on the Os sites that convert the system to $5d^2$ configuration. The formation of polarons, quasiparticles formed by the coupling of excess charge with ionic vibrations, has been recently proposed as another plausible mechanism for dopant trapping [24, 56].

Our magnetization measurements reveal that AF exchange interactions become enhanced as charge doping alters its configuration from $5d^1 \to 5d^2$. Furthermore, detailed analysis of the NMR shift and lineshapes in the magnetically ordered state reveals that magnetism coexists with the BLPS phase, and that it evolves from a canted AFM state to a collinear AF for dopant levels exceeding ($x > 0.1$). In $5d^1$ Ba_2NaOsO_6, a cAF order was identified to arise from the BLPS, as a result of the interplay of electron correlations and the degree of Jahn-Teller distortions [52]. That is, the collinear AF order cannot be stabilized in the absence of cubic symmetry in the $5d^1$ compound. Our finding that a collinear AF order coexists with the BLPS for $x > 0.1$ suggests that the theoretical results of [52] need to be extended to include effects of enhanced electron correlations, SOC, and Jahn-Teller interaction with doping. Therefore, our result show that charge doping profoundly alters the interplay between spin-exchange interactions, Jahn-Teller distortions, and electronic correlations as the system evolves away from the $5d^1$ configuration, and provides pertinent constraints to guide the development of microscopic models of Mott insulators with SOC.

Through a comprehensive analysis of the temperature dependence of the NMR shift and lineshapes, we established that a BLPS phase occupies an increasing portion of the $(H-T)$ phase diagram with increased doping. This finding is seemingly in contradiction with those in [21, 57] reporting a single transition into Néel order at $T^* \approx 50$ K, and no evidence of deviations from cubic symmetry in Ba_2CaOsO_6. It was proposed that these rather unusual results below T^* in [21] may be reconciled by the emergence of time-reversal symmetry breaking, ferro-octupolar order [17, 22, 49]. Although the diffraction data in [21] is high intensity, it is not obvious that its resolution was sufficient to detect a small deviations from cubic symmetry like those reported here and/or seen in Ba_2MgReO_6 [19]. Improved resolution in [57] might still not be good enough to detect a deviation from cubic symmetry. Moreover, it is possible that the local deviations from cubic symmetry in the BLPS, as reported here, are not sufficiently coherent to drive a long range distortion observable in scattering experiments. Indeed, an antiferro order of active quadrupoles within the e_g doublet was identified in [2] as a competing phase. If the distortions inherent to the BLPS phase are present, then the quadrupolar AFM phase is more stable. This is in contrast with the case when the system preserves cubic symmetry and acquires a octupolar-FM order. Since these two multipolar phases are very close in energy, it could be that small perturbation induce tiny local distortions and promote the onset of the quadrupolar AFM.

Our microscopic data clearly shows that in the limit of $x \to 1$, the system deviates from cubic symmetry below $T_{SB} \sim 80$ K, while a Néel AF order develops below $T_N \sim 30$ K, with a staggered moment of $0.05\,\mu_B$. Therefore, our observations of the broken local cubic symmetry indicate that the BLPS phase is driven by a formation of a multipolar order, most-likely of the antiferro-quadrupolar type [2, 3], because ferro-octupolar order preserves cubic symmetry. The conclusion that the BLPS phase is of antiferro-quadrupolar type is supported by two additional findings. Firstly, the BLPS phase is characterized by an anisotropic NMR shift tensor in addition to orthorhombic local distortions. Secondly, the alluded inhomogeneous nature of the charge doping promotes quadrupolar four-spin exchange interactions, making quadrupolar phase more stable, and implying that the onset of the BLPS-quadrupolar phase should occur at a higher temperature as doping increases, consistent with presented observations. Our NMR measurements indicate that local distortions, induced by the antiferro-quadrupolar order, are inhomogeneous, *i.e.* consists of areas of distortions of different magnitude. Such local distortions, seen by NMR, do not coherently order and give rise to diffraction peaks here in the way they do in the related $5d^1$ compound, Ba_2MgReO_6 [19].

One could argue that ferro-octupolar order is not observed in our doped samples simply because inhomogeneous dopants can induce local strain, consequently leading to a breaking of the local cubic symmetry. However, local strain is predicted to suppress the octupolar ordering temperature because it induces a transverse field in the octupolar ordering direction which promotes quantum fluctuations [22], and thus is in contradiction with phase diagram presented in Fig. 4. Therefore, our NMR findings support emergence of an antiferro-quadrupolar order in the doped $5d^1 \to 5d^2$ double perovskites. The quadrupolar phase most-likely arises as lattice distortions amplify the quadrupolar interactions via Jahn-Teller interactions.

Methods

Sample. The powder samples of $Ba_2Na_{1-x}Ca_xOsO_6$ investigated here are the same as in Ref. [23]. Powder x-ray diffraction (PXRD) measurements were performed to test the quality of the samples and analysed with Rietveld refinement. The compositional evolution of the lattice parameter is shown to follow Vegard's Law, indicating a successful Na/Ca substitution [23].

Muon spin resonance. All μSR measurements were performed at the General Purpose Surface-Muon Instrument at the Paul Scherrer Institute in Switzerland. In μSR measurements, spin-polarized muons implant in the powder samples and precess around the local magnetic field with a frequency given by $\nu = \gamma_\mu \cdot |\mathrm{B}|/2\pi$, where $\gamma_\mu = 2\pi \cdot 135.5$ MHz/T. The muons decay with a characteristic lifetime of 2.2 μs, emitting a positron, preferentially along the direction of the muon spin. The positrons are detected and counted by a forward $(N_F(t))$ and backward detector $(N_B(t))$, as a function of time. The asymmetry function A(t) is given by

$$A(t) = \frac{N_B(t) - \alpha N_F(t)}{N_B(t) + \alpha N_F(t)}, \tag{1}$$

where α is a parameter determined experimentally from the geometry and efficiency of the μSR detectors. $A(t)$ is proportional to the muon spin polarization, and thus reveals information about the local magnetic field sensed by the muons. A typical zero-field μSR spectra below and above the magnetic transition temperature for $Ba_2Na_{1-x}Ca_xOsO_6$ are presented in the Supplementary Material. The μSR spectra for all doping concentrations display damped oscillations at low temperatures (Supplementary Material 1), marking a transition to a state of long-range magnetic order. The spectra for the end elements, $x = 0$ and $x = 1$, are in agreement with those previously reported [42, 47]. Each individual spectrum was fitted to a sum of precessing and relaxing asymmetries given by

$$\begin{aligned} A(t) &= \left[\sum_{i=1}^{2} A_i e^{-\frac{\sigma_i^2 t^2}{2}} cos(2\pi\nu_i t) + A_3 e^{-\frac{\sigma_3^2 t^2}{2}} \right] \\ &\quad + A_\ell e^{-\frac{t}{T_1}}. \end{aligned} \tag{2}$$

The terms inside the brackets reflect the perpendicular component of the internal local field probed by the spin-polarized muons, the first term corresponds to the damped oscillatory muon precession about the local internal fields at frequencies ν_i, while the second reflects a more incoherent precession with a local field distribution given by σ. The term outside the brackets reflects the longitudinal component characterized by the relaxation rate T_1.

The development of a magnetic phase can be probed by measuring the volume of magnetic and non-magnetic regions within our sample. This magnetic volume fraction (V_{mag}) can be obtained from the longitudinal (A_ℓ) and total (A_{tot}) component of the polarized muons, given by the expression

$$V_{mag} = \frac{3}{2}\left(1 - \frac{A_\ell}{A_{tot}}\right). \tag{3}$$

Magnetization. Bulk magnetization measurements were performed using a superconducting quantum interference device (SQUID) magnetometer. Isothermal magnetization measurements as a function of applied field were performed at 2 K from -70 to 70 kOe. Zero-field and field-cooled magnetic susceptibility measurements were performed from 2 K to 400 K under an applied field of 1000 Oe.

NMR. NMR measurements were performed using high homogeneity superconducting magnets at Brown University, and the National High Magnetic Field Laboratory in Tallahassee, FL for magnetic fields exceeding 9 T. Temperature control was provided by ^{4}He variable temperature inserts. ^{23}Na NMR data ware collected using state-of-the-art, laboratory-made NMR spectrometers from the sum of spin-echo Fourier transforms recorded at constant frequency intervals. Pulse sequences of the form ($\pi/2 - \tau - \pi/2$) were used and none of the presented NMR observables depend on the duration of time interval τ.

^{23}Na NMR. ^{23}Na NMR is a powerful local probe of both the electronic spin polarization (local magnetism), via the hyperfine coupling between electronic magnetic moments and the ^{23}Na nuclear spin $I = 3/2$, and the charge distribution (orbital order and lattice symmetry), via the quadrupolar interaction between the electric field gradient (EFG) and the ^{23}Na quadrupole moment Q [1, 50]. They affect both the first and second moments of the frequency distribution, *i.e.* the NMR spectra.

The Knight shift. The Knight shift is defined as

$$K^i = (\omega^i - \omega_0)/\omega_0,$$

where $\omega_0 = {}^{23}\gamma \cdot H_0$, where ${}^{23}\gamma = 11.2625$ MHz/T and H_0 is the externally applied magnetic field, and ω^i is obtained from the first moment and/or peak position of the NMR spectral lines. This equation forms the general definition of the NMR shift K in terms of the observed NMR frequency, $\omega^i \equiv \gamma H_0(1 + K)$, where $K \equiv H_{loc}/H_0$ is the shift. Therefore, K is a measure of the relative strength of the component of the local magnetic field (H_{loc}) parallel to the applied magnetic field, H_0. In the more general case where the shift varies as a function of the orientation of H_0 (anisotropic shift), the scalar K is promoted to a second-rank tensor $\mathbb{K}$ and the expression for the observed NMR frequency becomes [58]

$$\omega^i = \gamma H_0(1 + \hat{\mathbf{h}} \cdot \mathbb{K} \cdot \hat{\mathbf{h}}), \tag{4}$$

where $\hat{\mathbf{h}} = \mathbf{H}_0/H_0$ is a unit vector in the direction of the applied magnetic field.

When the quadrupole interaction is taken into account, the observed NMR frequency becomes, $\omega^i = \gamma(1+K)H_0 + \omega_Q(m-1/2)\left(3\cos^2\theta_Q - 1 + \eta\sin^2\theta_Q\cos 2\varphi_Q\right)$ up to second order in perturbation theory [1, 50, 58]. The second term accounts for the quadrupole interaction for each $m \leftrightarrow m \pm 1$ transition and can be used to deduce the quadrupole parameters when the principal axes of the EFG tensor coincide with those of the crystal, as in the case of Ba$_2$NaOsO$_6$ [1]. Here, θ_Q and φ_Q are the angles between the applied field and the principal axes of the electric field gradient (EFG) defined so that $|V_{ZZ}| \geq |V_{XX}| \geq |V_{YY}|$ and $eq \equiv V_{ZZ}$. The asymmetry parameter η is set as $\eta \equiv (V_{XX} - V_{YY})/V_{ZZ}$. The quadrupolar frequency equals to $\omega_Q = 3e^2qQ/(\hbar 2I(2I-1))$, where Q and q are the nuclear and electronic quadrupole moments.

To relate the quadrupolar interaction effect to the observed NMR frequency, we introduce the quadrupolar splitting tensor $\mathbb{W}$, such that $\Delta\omega = \sum_\alpha W_\alpha \hat{h}_\alpha^2$ in the coordinate system O_{xyz}, where $\mathbb{W}$ is diagonal. Here O_{xyz} is defined by the crystalline axis of the cubic perovskite unit cell [50], $\alpha = \{x, y, z\}$, and $\hat{h}$ is the unit vector along the applied field.

In the presence of the anisotropic shift and quadrupolar interactions, the full expression for the observed NMR frequency becomes

$$\omega^i = \gamma H_0(1 + \hat{\mathbf{h}} \cdot \mathbb{K} \cdot \hat{\mathbf{h}} + \mathbb{W} \cdot \hat{\mathbf{h}}^2). \tag{5}$$

Calculation of NMR spectra below T_N. In the magnetically ordered phase, we model the local magnetic field at a Na site as $H_{loc} = \hat{\mathbf{h}} \cdot \sum_i \mathbb{A}_i \cdot \vec{S}_i$, where $\hat{\mathbf{h}}$ is a unit vector in the applied field direction, $\mathbb{A}_i$ is the hyperfine coupling tensor with the i^{th} nearest-neighbour Os atom, and $\vec{S}_i$ is its local spin moments. We note that contributions from dipolar effects are relatively small and are thus neglected. By performing a full lattice sum, we calculate the local fields projected in the direction of the applied field at the Na sites for the entire single crystal. The corresponding NMR spectra is a histogram of these local fields. The powder spectrum is then obtained by rotating the $\hat{\mathbf{h}}$ over the solid angle and integrating the results (see Supplementary Note 4). The diagonal components of the hyperfine tensor are optimized based on the hyperfine coupling values obtained from the NMR Knight shift and magnetic susceptibility measurements (see Supplementary Figure 4), while the symmetry of the hyperfine tensor is assumed to be the same as that found in the single crystal Ba_2NaOsO_6 [1]. The quadrupolar broadening effects are accounted for utilizing EFG parameters determined from the intermediate temperature powder spectrum simulation (see Supplementary Note 4).

Transition temperature. The transition temperature (T_N) from the PM to low-temperature magnetically ordered state was determined by examining the magnetic volume fraction V_{mag} from zero-field μSR, and in finite fields from the temperature dependence of the NMR observables. That is, T_N^{μ} is delineated as a temperature at which V_{mag} exceeds 90%. From NMR analysis, T_N is defined as the onset temperature of a significant drop in the Knight shift associated with the formation of the AF ordering. Such T_N is consistent with the one determined from the peak of the NMR relaxation rate, induced by critical fluctuations when approaching a transition into a long-range ordered magnetic state as a function of temperature.

The onset temperature for the breaking of local cubic symmetry, T_{SB}, was identified by the bifurcation in $1/|K|\, vs. T$ between the shifts defined relative to ω^i, corresponding to the peak position ($i = pp$) and first moment ($i = fm$).

ACKNOWLEDGEMENTS

We are thankful to D. Fiore Mosca, P. Santini, Brad Marston, and A. Paramekanti for enlightening discussions. This work was supported in part by U.S. National Science Foundation (NSF) grant No. DMR-1905532 (V.F.M.), the NSF Graduate Research Fellowship under Grant No. 1644760 (E.G.), NSF Materials Research Science and Engineering Center (MRSEC) Grant No. DMR-2011876 (P.M.T. and P.M.W.), and University of Bologna (S.S. and P.C.F.). Part of this work is based on experiments performed at the Swiss Muon Source SμS, Paul Scherrer Institute, Villigen, Switzerland. The study at the NHMFL was supported by the National Science Foundation under Cooperative Agreement no. DMR-1644779 and the State of Florida.

AUTHOR CONTRIBUTIONS

E.G., R.C., P.C.F., A.T. , A. P. R. and G.A. obtained NMR data and performed the data analysis. S.S. lead the muon spin spectroscopy experiment for which E.G. and R.C. contributed equally to data acquisition and interpretations. P.M.T. and P.M.W. grew the samples and performed the magnetic susceptibility measurement. S.S., V.F.M. and C.F. ideated the project. S.S. and V.F.M. supervised the experiments, lead data analysis and interpretations and writing of the manuscript. R.C., G.A., and V.F.M. were involved in the simulations of the NMR data. C.F. performed first principle calculations and was involved in data interpretations. A.P.R. enabled all measurements above 10 T at the NHMFL. All authors have read the paper and approved it. All authors discussed the results and commented on and edited the manuscript.

[1] L. Lu, M. Song, W. Liu, A. P. Reyes, P. Kuhns, H. O. Lee, I. R. Fisher, and V. F. Mitrović. Magnetism and local symmetry breaking in a Mott insulator with strong spin orbit interactions. Nature Communications, 8:14407 EP –, 02 2017.

[2] Giniyat Khaliullin, Derek Churchill, P. Peter Stavropoulos, and Hae-Young Kee. Exchange interactions, Jahn-Teller coupling, and multipole orders in pseudospin one-half $5d^2$ Mott insulators. Phys. Rev. Research, 3:033163, Aug 2021.

[3] Derek Churchill and Hae-Young Kee. Competing multipolar orders in a face-centered cubic lattice: Application to the osmium double perovskites. Phys. Rev. B, 105:014438, Jan 2022.

[4] William Witczak-Krempa, Gang Chen, Yong Baek Kim, and Leon Balents. Correlated quantum phenomena in the strong spin-orbit regime. Annu. Rev. Condens. Matter Phys., 5(1):57–82, 2014.

[5] G Jackeli and G Khaliullin. Mott insulators in the strong spin-orbit coupling limit: from Heisenberg to a quantum compass and Kitaev models. Physical Review Letters, 102(1):017205, 2009.

[6] F. O. Nigmatulin, I. A. Shelykh, and I. V. Iorsh. Quantum spin compass models in two-dimensional electronic topological metasurfaces. Phys. Rev. Research, 3:043016, Oct 2021.

[7] Tomohiro Takayama, Jiří Chaloupka, Andrew Smerald, Giniyat Khaliullin, and Hidenori Takagi. Spin–Orbit-Entangled Electronic Phases in 4d and 5d Transition-Metal Compounds. Journal of the Physical Society of Japan, 90(6):062001, 2021.

[8] Gang Chen, Rodrigo Pereira, and Leon Balents. Exotic phases induced by strong spin-orbit coupling in ordered double perovskites. Phys. Rev. B, 82:174440, Nov 2010.

[9] Gang Chen and Leon Balents. Spin-orbit coupling in d^2 ordered double perovskites. Physical Review B, 84(9):094420, September 2011.

[10] Christopher Svoboda, Wenjuan Zhang, Mohit Randeria, and Nandini Trivedi. Orbital order drives magnetic order in $5d^1$ and $5d^2$ double perovskite Mott insulators. Physical Review B, 104(2):024437, 2021.

[11] Hiroaki Ishizuka and Leon Balents. Magnetism in $S = 1/2$ double perovskites with strong spin-orbit interactions. Physical Review B, 90(18):184422, 2014.

[12] Rong Cong and Vesna F. Mitrović. Monte Carlo simulation of a strong SOC model for $5d^1$ double perovskite. Bulletin of the American Physical Society, 2021.

[13] Erik S. Sørensen, Andrei Catuneanu, Jacob S. Gordon, and Hae-Young Kee. Heart of Entanglement: Chiral, Nematic, and Incommensurate Phases in the Kitaev-Gamma Ladder in a Field. Phys. Rev. X, 11:011013, Jan 2021.

[14] Qiang Luo, P. Peter Stavropoulos, Jacob S. Gordon, and Hae-Young Kee. Spontaneous chiral-spin ordering

in spin-orbit coupled honeycomb magnets. Phys. Rev. Research, 4:013062, Jan 2022.

[15] A. S. Cavichini, M. T. Orlando, J. B. Depianti, J. L. Passamai, F. Damay, F. Porcher, and E. Granado. Exotic magnetism and spin-orbit-assisted Mott insulating state in a $3d - 5d$ double perovskite. Phys. Rev. B, 97:054431, Feb 2018.

[16] Aria Mansouri Tehrani and Nicola A. Spaldin. Untangling the structural, magnetic dipole, and charge multipolar orders in Ba_2MgReO_6. Phys. Rev. Materials, 5:104410, Oct 2021.

[17] Arun Paramekanti, Dalini D Maharaj, and Bruce D Gaulin. Octupolar order in d-orbital Mott insulators. Physical Review B, 101(5):054439, 2020.

[18] Sreekar Voleti, Dalini D Maharaj, Bruce D Gaulin, Graeme Luke, and Arun Paramekanti. Multipolar magnetism in d-orbital systems: Crystal field levels, octupolar order, and orbital loop currents. Physical Review B, 101(15):155118, 2020.

[19] Daigorou Hirai, Hajime Sagayama, Shang Gao, Hiroyuki Ohsumi, Gang Chen, Taka-hisa Arima, and Zenji Hiroi. Detection of multipolar orders in the spin-orbit-coupled $5d$ Mott insulator Ba_2MgReO_6. Phys. Rev. Research, 2:022063, Jun 2020.

[20] R. D. Johnson, I. Broeders, K. Mehlawat, Y. Li, Yogesh Singh, R. Valentí, and R. Coldea. Chemical tuning between triangular and honeycomb structures in a $5d$ spin-orbit Mott insulator. Phys. Rev. B, 100:214113, Dec 2019.

[21] Dalini D Maharaj, Gabriele Sala, Matthew B Stone, Edwin Kermarec, Clemens Ritter, François Fauth, Casey A Marjerrison, John E Greedan, Arun Paramekanti, and Bruce D Gaulin. Octupolar versus Néel Order in Cubic $5d^2$ Double Perovskites. Physical Review Letters, 124(8):087206, 2020.

[22] Sreekar Voleti, Arijit Haldar, and Arun Paramekanti. Octupolar order and Ising quantum criticality tuned by strain and dimensionality: Application to d-orbital Mott insulators. Physical Review B, 104(17):174431, 2021.

[23] Jagadesh Kopula Kesavan, Dario Fiore Mosca, Samuele Sanna, Francesco Borgatti, Gotz Schuck, Phuong Minh Tran, Patrick M Woodward, Vesna F Mitrović, Cesare Franchini, and Federico Boscherini. Doping Evolution of the Local Electronic and Structural Properties of the Double Perovskite $Ba_2Na_{1-x}Ca_xOsO_6$. The Journal of Physical Chemistry C, 124(30):16577–16585, 2020.

[24] Lorenzo Celiberti, Dario Fiore Mosca, Anna Tassetti, Paola Caterina Forino, Roberto De Renzi, Giuseppe Allodi, Vesna Mitrović, Erick Garcia, Rong Cong, Patrick Woodward, Samuele Sanna, and Cesare Franchini. Small polaron formation in $5d$ spin-orbit coupled omsates. Bulletin of the American Physical Society, D70.00007, 2022.

[25] Masatoshi Imada, Atsushi Fujimori, and Yoshinori Tokura. Metal-insulator transitions. Rev. Mod. Phys., 70:1039–1263, Oct 1998.

[26] Patrick A Lee, Naoto Nagaosa, and Xiao-Gang Wen. Doping a Mott insulator: Physics of high-temperature superconductivity. Reviews of Modern Physics, 78(1):17, 2006.

[27] Zi-Xiang Li, Steven A. Kivelson, and Dung-Hai Lee. Superconductor-to-metal transition in overdoped cuprates. npj Quantum Materials, 6(1):36, 2021.

[28] Hong-Chen Jiang and Steven A. Kivelson. Stripe order enhanced superconductivity in the Hubbard model. Proceedings of the National Academy of Sciences, 119(1):e2109406119, 2022.

[29] Eduardo Fradkin, Steven A. Kivelson, and John M. Tranquada. Colloquium: Theory of intertwined orders in high temperature superconductors. Rev. Mod. Phys., 87:457–482, May 2015.

[30] Srimanta Middey, Jak Chakhalian, P Mahadevan, JW Freeland, Andrew J Millis, and DD Sarma. Physics of ultrathin films and heterostructures of rare-earth nickelates. Annual Review of Materials Research, 46:305–334, 2016.

[31] Y Tokura and N Nagaosa. Orbital physics in transition-metal oxides. Science, 288(5465):462–468, 2000.

[32] Weiren Xia, Zhipeng Pei, Kai Leng, and Xinhua Zhu. Research progress in rare earth-doped perovskite manganite oxide nanostructures. Nanoscale Research Letters, 15(1):1–55, 2020.

[33] Yejun Feng, Yishu Wang, D. M. Silevitch, S. E. Cooper, D. Mandrus, Patrick A. Lee, and T. F. Rosenbaum. A continuous metal-insulator transition driven by spin correlations. Nature Communications, 12(1):2779, 2021.

[34] Jean-Michel Carter, Hae-Young Kee, et al. Theory of metal-insulator transition in the family of perovskite iridium oxides. Physical Review B, 88(3):035111, 2013.

[35] Tao Han, Yongjian Wang, Jun Yang, Lei He, Junmin Xu, Dandan Liang, Hui Han, M Ge, CY Xi, WK Zhu, et al. Enhanced electrical conductivity and diluted Ir^{4+} spin orders in electron doped iridates $Sr_{2-x}Ga_xIrO_4$. Applied Physics Letters, 109(19):192409, 2016.

[36] Abhisek Bandyopadhyay, Ilaria Carlomagno, Laura Simonelli, M Moretti Sala, A Efimenko, Carlo Meneghini, and Sugata Ray. Evolution of electronic and magnetic properties in a series of iridate double perovskites $Pr_{2-x}Sr_xMgIrO_6$ (x= 0, 0.5, 1.0). Physical Review B, 100(6):064416, 2019.

[37] M Vogl, LT Corredor, T Dey, R Morrow, F Scaravaggi, AUB Wolter, S Aswartham, S Wurmehl, and B Büchner. Interplay of 3 d-and 5 d-sublattice magnetism in the double perovskite substitution series $La_2Zn_{1-x}Co_xIrO_6$. Physical Review B, 97(3):035155, 2018.

[38] Yuxia Gao, Malik Ashtar, Longmeng Xu, Zhongwen Ouyang, Wei Tong, Songliu Yuan, and Zhaoming Tian. The effect of carrier doping on magnetism and electronic behavior in double perovskite La_2ZnIrO_6. Journal of Physics: Condensed Matter, 32(10):105702, 2019.

[39] N Narayanan, D Mikhailova, A Senyshyn, DM Trots, R Laskowski, P Blaha, K Schwarz, H Fuess, and H Ehrenberg. Temperature and composition dependence of crystal structures and magnetic and electronic properties of the double perovskites $La_{2-x}Sr_xCoIrO_6$ ($0 < x < 2$). Physical Review B, 82(2):024403, 2010.

[40] WK Zhu, Chi-Ken Lu, W Tong, JM Wang, HD Zhou, and SX Zhang. Strong ferromagnetism induced by canted antiferromagnetic order in double perovskite iridates $(La_{1-x}Sr_x)_2ZnIrO_6$. Physical Review B, 91(14):144408, 2015.

[41] Katharine E Stitzer, Mark D Smith, and Hans-Conrad zur Loye. Crystal growth of Ba_2MOsO_6 (M= Li, Na) from reactive hydroxide fluxes. Solid State Sciences, 4(3):311–316, 2002.

[42] Andrew J Steele, Peter J Baker, Tom Lancaster, Francis L Pratt, Isabel Franke, Saman Ghannadzadeh, Paul A Goddard, William Hayes, D Prabhakaran, and Stephen J

Blundell. Low-moment magnetism in the double perovskites Ba_2MOsO_6 (M= Li, Na). Physical Review B, 84(14):144416, 2011.

[43] AS Erickson, Sumohan Misra, Gordon J Miller, RR Gupta, Z Schlesinger, WA Harrison, JM Kim, and IR Fisher. Ferromagnetism in the Mott insulator Ba_2NaOsO_6. Physical Review Letters, 99(1):016404, 2007.

[44] W. Liu, R. Cong, E. Garcia, A. P. Reyes, H. O. Lee, I. R. Fisher, and V. F. Mitrović. Phase Diagram of Ba_2NaOsO_6, a Mott insulator with strong spin orbit interactions. Physica B: Condensed Matter, 536:863 – 866, 2018.

[45] R. Cong, Ravindra Nanguneri, Brenda Rubenstein, and V. F. Mitrović. Evidence from first-principles calculations for orbital ordering in Ba_2NaOsO_6: A Mott insulator with strong spin-orbit coupling. Phys. Rev. B, 100:245141, Dec 2019.

[46] Kazuhiro Yamamura, Makoto Wakeshima, and Yukio Hinatsu. Structural phase transition and magnetic properties of double perovskites Ba_2CaMO_6 (M= W, Re, Os). Journal of solid state chemistry, 179(3):605–612, 2006.

[47] CM Thompson, JP Carlo, R Flacau, T Aharen, IA Leahy, JR Pollichemi, TJS Munsie, T Medina, GM Luke, J Munevar, et al. Long-range magnetic order in the $5d^2$ double perovskite Ba_2CaOsO_6: comparison with spin-disordered Ba_2YReO_6. Journal of Physics: Condensed Matter, 26(30):306003, 2014.

[48] SW Lovesey and DD Khalyavin. Lone octupole and bulk magnetism in osmate $5d^2$ double perovskites. Physical Review B, 102(6):064407, 2020.

[49] Leonid V Pourovskii, Dario Fiore Mosca, and Cesare Franchini. Ferro-octupolar Order and Low-Energy Excitations in d^2 Double Perovskites of Osmium. Physical Review Letters, 127(23):237201, 2021.

[50] W. Liu, R. Cong, A. P. Reyes, I. R. Fisher, and V. F. Mitrović. Nature of lattice distortions in the cubic double perovskite Ba_2NaOsO_6. Phys. Rev. B, 97:224103, Jun 2018.

[51] Rong Cong, Ravindra Nanguneri, Brenda Rubenstein, and V. F. Mitrović. First principles calculations of the electric field gradient tensors of Ba_2NaOsO_6, a Mott insulator with strong spin orbit coupling. Journal of Physics: Condensed Matter, 32(40):405802, 2020.

[52] Dario Fiore Mosca, Leonid V. Pourovskii, Beom Hyun Kim, Peitao Liu, Samuele Sanna, Federico Boscherini, Sergii Khmelevskyi, and Cesare Franchini. Interplay between multipolar spin interactions, Jahn-Teller effect, and electronic correlation in a $J_{\mathrm{eff}} = \frac{3}{2}$ insulator. Phys. Rev. B, 103:104401, Mar 2021.

[53] Judit Romhányi, Leon Balents, and George Jackeli. Spin-Orbit Dimers and Noncollinear Phases in d^1 Cubic Double Perovskites. Phys. Rev. Lett., 118:217202, May 2017.

[54] Dario Fiore Mosca, Leonid V. Pourovskii, and Cesare Franchini. Modeling magnetic multipolar phases in density functional theory. Phys. Rev. B, 106:035127, Jul 2022.

[55] M-A Vachon, G Koutroulakis, V F Mitrović, A P Reyes, P Kuhns, R Coldea, and Z Tylczynski. Anisotropic transferred hyperfine interactions in Cs_2CuCl_4. Journal of Physics: Condensed Matter, 20(29):295225, 2008.

[56] Cesare Franchini, Michele Reticcioli, Martin Setvin, and Ulrike Diebold. Polarons in materials. Nature Reviews Materials, 6(7):560–586, 2021.

[57] C. M. Thompson *et al.* Long-range magnetic order in the 5d2 double perovskite Ba_2CaOsO_6: comparison with spin-disordered Ba_2YReO_6. Journal of Physics: Condensed Matter, 26(30):306003, 2014.

[58] A. Abragam. The principles of Nuclear Magnetism. Oxford University Press, 1961.